Characterization of a neutron sensitive MCP/Timepix detector for quantitative image analysis at a pulsed neutron source

Watanabe, Kenichi
Nagoya University

Minniti, Triestino
STFC, Rutherford Appleton Laboratory, ISIS Facility

Kockelmann, Winfried
STFC, Rutherford Appleton Laboratory, ISIS Facility

Dalgliesh, Robert
STFC, Rutherford Appleton Laboratory, ISIS Facility

他

出版情報：Nuclear Instruments and Methods in Physics Research Section A: Accelerators, Spectrometers, Detectors and Associated Equipment. 861, pp.55-63, 2017-07-21. Elsevier
バージョン：
権利関係：

Characterization of a neutron sensitive MCP/Timepix detector for quantitative image analysis at a pulsed neutron source

Kenichi Watanabe[1], Triestino Minniti[2], Winfried Kockelmann[2], Robert Dalgliesh[2], Genoveva Burca[2], Anton S. Tremsin[3]

[1] Nagoya University, Furo-cho, Chikusa-ku, Nagoya, 464-8603, Japan

[2] STFC, Rutherford Appleton Laboratory, ISIS Facility, Harwell, OX11 0QX, United Kingdom

[3] Space Science Laboratory, University of California at Berkeley, CA 94720 Berkeley, U.S.A.

Email of corresponding author: k-watanabe@nucl.nagoya-u.ac.jp

Abstract

The uncertainties and the stability of a neutron sensitive MCP/Timepix detector when operating in the event timing mode for quantitative image analysis at a pulsed neutron source were investigated. The dominant component to the uncertainty arises from the counting statistics. The contribution of the overlap correction to the uncertainty was concluded to be negligible from considerations based on the error propagation even if a pixel occupation probability is more than 50%. We, additionally, have taken into account the multiple counting effect in consideration of the counting statistics. Furthermore, the detection efficiency of this detector system changes under relatively high neutron fluxes due to the ageing effects of current Microchannel Plates. Since this efficiency change is position-dependent, it induces a memory image. The memory effect can be significantly reduced with correction procedures using the rate equations describing the permanent gain degradation and the scrubbing effect on the inner surfaces of the MCP pores.

KEYWORDS: *microchannel plate, neutron imaging detector, time-of-flight measurement, energy resolved imaging*

1. Introduction

Energy resolved neutron imaging is an emerging method which is likely to expand the capabilities the analysis options of neutrons in materials science. Energy resolved images can effectively be acquired by combining a pulsed neutron source and a time-resolving camera by using the neutron time-of-flight (TOF) method. Pulsed neutron source facilities have built or are preparing to build instruments for energy selective neutron imaging, such as RADEN in J-PARC and IMAT in ISIS, which is just now under commissioning [1-3]. These instruments have a relatively high neutron fluxes of more than 10^7 neutrons/cm^2/s. Therefore, the requirements for neutron imaging detectors include not only time-resolving capabilities but also stability under high neutron flux operation. Since at present the performance of the time-resolved neutron imaging systems does not fully meet requirements for operations at pulsed neutron sources [4], many detectors for this purpose are being developed. A promising candidate is a borated-microchannel plate (MCP) detector combined with Timepix chip, which is a high performance application-specific integrated circuit (ASIC) readout chip [5-6]. This type of detector, now being installed at the ISIS pulsed neutron source as the time-resolving neutron imaging camera, is a position sensitive neutron counting detector with 55μm pixel size, with 512x512 pixels active area. The relatively small pixel size of the Timepix chip reduces count rates per pixel to a moderate level. Thus, this detector can operate under high flux conditions [7-8] and also perform time-resolved detection of each neutron using the event timing mode of the Timepix chip [5-6].

Due to its spatial and time resolving capabilities, the MCP/Timepix detector has been considered and used for a wide range of neutron applications, such as neutron resonance transmission imaging and stress mapping via Bragg-edge analysis [9-10]. In these applications, shape information of TOF spectra, such as profiles and positions of resonances or Bragg-edges, is more important than measuring accurate transmittance values. Therefore, quantitative evaluation of detected neutron counts in the MCP/Timepix detector has hardly been discussed so far. In this paper, we discuss the uncertainties and stability on the MCP/Timepix detector under operating conditions at a pulsed neutron source, which are important characteristics to perform quantitative neutron transmission analyses.

For counting detectors, the count rate uncertainty is considered mainly based on counting statistics or

Poisson statistics. However, under relatively high neutron flux situation, the MCP/Timepix system has severe counting loss or dead time effects based on the overlap effect [11]. Since this effect distorts the TOF spectrum shape, a correction procedure as proposed by A.S. Tremsin et al. [11] is essential. Here we consider the uncertainties of this correction procedure.

In energy-resolved imaging, neutrons are shared across a large number of energy channels. This means that each measurement usually requires relatively long acquisition times, typically of the order of many hours. Neutron imaging requires 'flat field' or 'open beam' measurements for normalization purposes to correct for spatial and temporal non-uniformities of neutron beam intensity and detector sensitivities. These open beam measurements are time-consuming, and hence time-stability is one of the essential characteristics of a neutron imaging camera. The MCP/Timepix detector satisfies the requirements for stable operation under relatively low neutron fluxes. The IMAT beamline adopted the MCP/Timepix detector as one of the neutron imaging detectors. However, for operation on relatively high neutron flux instruments, such as RADEN and IMAT, the long term stability of the detector should be confirmed for full-scale operation. These aspects will be extensively addressed in this paper.

2. Camera system and experimental set-up

2.1 Neutron sensitive MCP/Timepix detector

The position sensitive photon, ion and neutron counting capabilities of MCP detectors have been demonstrated previously with several readout technologies [12-14]. The neutron sensitive MCP used in this work contains boron and gadolinium in the glass matrix. Boron atoms work as a converter from slow neutrons to energetic charged particles, such as alphas and ^{7}Li ions through ^{10}B(n, α)^{7}Li reactions. When these energetic particles impact onto inner surface of MCP pores, several electrons are emitted. The emitted electrons are multiplied by the MCP and are detected by readout components. Since these multiplied electrons are confined within a MCP pore, position sensitive detection up to the limit of the pore-to-pore spacing is achieved by using position-sensitive readout electronics. The neutron sensitive MCP detector discussed here employs the Timepix readout chip, paired with Medipix2 and developed at CERN [15].

The present detector consists of a chevron stack of MCPs positioned at 0.8 mm distance from Timepix ASIC readout [6]. The Timepix chip has 256x256 pixels with 55 μm pixel size. Each pixel has a preamplifier and can be operated at the rate of 100kHz/pixel. The readout of the present neutron sensitive MCP/Timepix detector used a 2x2 array of the Timepix chips with approximately 180 μm gap between each chip. This means the detector has 512x512 pixels and the field of view is 28x28 mm^2 in total. The top MCP, which is neutron sensitive and manufactured by Nova Scientific, Inc., is 50 mm in diameter, 0.8 mm thick and has 8 μm pores hexagonally packed with 10.5 μm pitch. The bottom MCP, which is just for electron multiplication and manufactured by Hamamatsu Photonics, are 5 cm in diameter, 0.6 mm thick and have 10 μm pores with 12 μm pitch. The applied voltage to the MCP stack was 2550 V for the data used in this paper.

The Timepix ASICs has three data acquisition modes; event counting mode, event timing mode and event centroiding mode. For energy-resolved imaging, we can apply the event timing mode, in which the time of arrival of individual neutron signals relative to trigger signals is measured. Each pixel in the Timepix has a 14 bit register, which is used to store the timing information before it is transferred to the data processing unit, which is based on field-programmable gate arrays (FPGA). The data readout takes places at the end of every 'shutter period', which is an arbitrarily adjustable data acquisition period in a pulsed source time frame (i.e. between successive proton/neutron pulses of the source). Multiple shutter periods can also be defined in a frame. The data transfer from the Timepix to the FPGA requires 320 μs to complete for all pixel data. The following unit creates three dimensional histograms, with two dimensions in space and one dimension in time of flight, based on the transferred data. Since only one event can be stored in each pixel for a given shutter period, second or subsequent events are rejected until data are transferred at the end of the shutter period. The case of an occupied pixel during the shutter period constitutes an overlap effect which induces dead time or counting loss. The TOF spectrum shape could be severely distorted under high flux conditions. The overlap effect can be alleviated by either implementation of shorter acquisition shutters or reducing the neutron flux. The MCP/Timepix system used here can be set-up with a total of 250 shutters. When the lengths of the individual shutter periods are shortened a larger number of readout sequences is to be

performed for each neutron pulse. During these 320 μs data transfer gaps, no data are recorded, introducing the larger number of gaps in the measured spectra. Hence the number and positions of the shutter periods need to be carefully selected.

2.2. Experimental setup

Characterization tests described in this paper were performed on the Larmor beamline in ISIS. The Larmor is one of the beamlines of ISIS Target Station 2 (TS2), which operates with 10 Hz repetition rate. This beamline is fundamentally a multi-purpose instrument for small angle neutron scattering (SANS), diffraction and spectroscopy utilizing the larmor precession of polarized neutrons. However, since the beam size of the Larmor is roughly 30x30mm^2, it can be used as a test beamline for the MCP detector, which has 28x28mm^2 sensitive area. This beamline also has a similar neutron spectrum to the neutron imaging beamline IMAT because it views the same coupled hydrogen moderator. The both beamlines have the maximum neutron intensity around 3 angstroms in wavelength. In these tests, the flight path between the neutron source and the MCP/Timepix detector was roughly 26 m. At that position, the neutron flux was approximately 5x10^6 n/cm^2/s.

3. Uncertainty in time-resolved mode

3.1 Overlap correction

As described above, the MCP/Timepix detectors suffer from the overlap effect when operating in a time-resolved mode, which is related to the fact that only event per pixel can be registered. Figure 1 shows an example of TOF spectra obtained at Larmor with the neutron sensitive MCP/Timepix detector. These are open beam or flat field TOF spectra, which were obtained without any sample. In this case, the neutron flux was approximately 5x10^6 n/cm^2/s and the data readout was divided into three shutter periods. The TOF spectrum was severely distorted and has significant discontinuous points at the readout gaps due to the overlap effect. However, this distortion can be corrected with the method proposed by A.S. Tremsin et al.[11]. The corrected TOF spectrum is also plotted in Fig. 1.

Here, we discuss procedures of the overlap correction. This correction technique can only be applied to the experiments where neutron pulses with periodical and constant shape are irradiated in each measurement, such as time of flight experiments with pulsed neutron sources and static objects. In the event timing mode of the Timepix chip, only one event per pixel can be stored in a register for a given shutter period or each readout period, because of the way the Timepix of current generation determines the time of event through the clock counter. This means that the following events are rejected in an already occupied pixel with a previous event until the register is refreshed. The occupied pixel is considered to be a dead pixel. However, for neutron pulses with periodical and constant shape, the pixel occupied probability at a given timing $P_{ocp}(t_i)$ can be predicted from the measured data themselves using

$$P_{ocp}(t_i) = \frac{\sum_{j=0}^{i-1} C(t_j)}{S} \quad (1),$$

where $C(t_i)$ is a recorded neutron count in the time bin of $t= t_i$ at a given pixel for S neutron pulses. In the time period from the beginning of the shutter t_0 to t_{i-1}, the pixel is occupied $\sum_{j=0}^{i-1} C(t_j)$ times for S trials or pulses. We would like to determine the real neutron counts $N(t_i)$ without the overlap loss. Since only neutron events entering into unoccupied pixels can be recorded, the real neutron counts $N(t_i)$ are written by

$$N(t_i) = \frac{C(t_i)}{P_{free}(t_i)} = \frac{C(t_i)}{1 - \frac{\sum_{j=0}^{i-1} C(t_j)}{S}} = f\, C(t_i) \quad (2),$$

where $P_{free}(t_i)$ is the probability not occupied pixel with the previous event or the free pixel probability. f is the overlap correction factor and defined as

$$f = \left(1 - \sum_{j=0}^{i-1} C(t_j) \Big/ S\right)^{-1} = \frac{1}{1 - P_{ocp}(t_i)} \quad (3).$$

The corrected TOF spectrum shown in Fig. 1 was obtained with this correction procedure. The pixel occupied probability $P_{ocp}(ti)$ is also plotted in Fig. 1. In this case, although the occupied probability is more than 50% at the maximum, the corrected spectrum is smoothly connected at the gaps and this correction

seems to work properly.

Next, we discuss the uncertainty in this correction procedure. The uncertainty of the correction factor *f* is derived from Eq. (3) as following:

$$\sigma_f = \left(1 - \sum_{j=0}^{i-1} C(t_j) \Big/ S\right)^{-2} \frac{\sigma_{\sum C(t)}}{S} \quad (4),$$

where $\sigma_{\sum C(t)}$ is the uncertainty of $\sum_{j=0}^{i-1} C(t_j)$. $\sum_{j=0}^{i-1} C(t_j)$ is the integrated neutron counts in the period from $t=t_0$ to t_{i-1} for S trials. For each trial or each neutron pulse, the event counting probability is $p = \sum_{j=0}^{i-1} C(t_j) \Big/ S$. Based on the Binominal distribution with the event occurring probability *p* and *S* trials, the average and the standard deviation of the number of event occurring are *Sp* and $\sqrt{Sp(1-p)}$, respectively. Therefore, $\sigma_{\sum C(t)}$ is written as

$$\sigma_{\sum C(t)} = \sqrt{\sum_{j=0}^{i-1} C(t_j) \left(1 - \sum_{j=0}^{i-1} C(t_j) \Big/ S\right)} \quad (5).$$

Note that the event occurring probability *p* might be relatively high under high neutron flux conditions and the counting statistics should be considered based on the Binominal distribution rather than Poisson statistics. Consequently, the relative uncertainty of the corrected factor *f* is written as

$$\frac{\sigma_f}{f} = \frac{\sqrt{\sum_{j=0}^{i-1} C(t_j)}}{S\sqrt{1 - \sum_{j=0}^{i-1} C(t_j) \Big/ S}} \quad (6).$$

We would like to know the contribution of this correction factor to the real or corrected neutron counts $N(t_i)$. The uncertainty of the corrected neutron counts is derived from Eq. (2) using:

$$\frac{\sigma_N}{N(t_i)} = \sqrt{\left(\frac{\sigma_C}{C(t_i)}\right)^2 + \left(\frac{\sigma_f}{f}\right)^2} \quad (7),$$

where $\sigma_C / C(t_i)$ is the relative uncertainty of the recorded counts and written by $1/\sqrt{C(t_i)}$ based on the

Poisson statistics. The relative contribution of the correction factor to the counting statistics into the uncertainty is written as

$$\frac{\frac{\sigma_f}{f}}{\frac{\sigma_C}{C(t_i)}} = \sqrt{\frac{\sum_{j=0}^{i-1} C(t_j)}{S^2\left(1-\sum_{j=0}^{i-1} C(t_j)/S\right)}} \Bigg/ \frac{1}{C(t_i)} = \sqrt{\frac{N(t_i)}{S} P_{ocp}(t_i)} \qquad (8).$$

Finally, we can obtain the following equation:

$$\frac{\sigma_N}{N(t_i)} = \frac{\sigma_C}{C(t_i)} \sqrt{1+\frac{N(t_i)}{S} P_{ocp}(t_i)} \qquad (9).$$

In this equation, the second term in the square root stands for contribution of the overlap correction. Although the contribution depends on the pixel occupation probability $P_{ocp}(t_i)$, the maximum contribution is $N(t_i)/S$, which is usually quite small, even if pixels are fully occupied. This equation suggests that the uncertainty contribution from the overlap correction is quite small and negligible under typical neutron flux conditions at ISIS, in which the detector can be normally operated.

3.2 Multiple counting effect

When considering the counting statistics in the MCP/Timepix detector, we also have to take into account the multiple counting effect, in which a single neutron might induce multiple counting events in the Timepix. In the neutron sensitive MCP/Timepix detector, the multiplied electron cloud in the MCP might spread over several neighboring pixels before reaching the Timepix chip. In the event timing mode, the events exceeding the threshold signal level are counted. The multiple counting occurs when signals in neighboring pixels exceeds the threshold simultaneously. Figure 2 shows an example image of the multiple counting effect, in which separately distributed neutron events can be seen due to its quite short acquisition time. Some spots consist of not only one pixel but also neighboring two or three pixels. The counting statistics based on Poisson statistics should be considered for the number of events. However, the apparent

recorded counts is larger than the real neutron events. This means that the expected relative statistical uncertainty from the recorded counts becomes smaller than the real one.

Since the amount of electron cloud for each neutron event depends on an interaction position of $^{10}B(n,\alpha)^{7}Li$ and Gd reaction along the pore, leading to a variation in gain, the number of shared pixels has a certain distribution. Under the MCP setting used in this paper, the number of shared pixel or spot size in each event M was determined to be 1.7 pixels on average with the standard deviation of 1.1 pixels. Since the apparent recorded counts C is the product of the average spot size $\langle M \rangle$ and the real number of neutron events N, the relative uncertainty of C is written as:

$$\frac{\sigma_C}{C} = \sqrt{\left(\frac{\sigma_{\langle M \rangle}}{\langle M \rangle}\right)^2 + \left(\frac{\sigma_N}{N}\right)^2} \quad (10),$$

where $\sigma_{\langle M \rangle}$ is the standard deviation of the average spot size but not the one of each spot size σ_M. Since $\langle M \rangle$ is the average of each spot size M_i (i=1, 2,…, N) for N spots, $\sigma_{\langle M \rangle}$ is given as:

$$\sigma_{\langle M \rangle} = \frac{\sigma_M}{\sqrt{N}} \quad (11).$$

Therefore, we can modify Eq. (10) as follows:

$$\frac{\sigma_C}{C} = \sqrt{\left(\frac{\sigma_{\langle M \rangle}}{\langle M \rangle}\right)^2 + \left(\frac{\sigma_N}{N}\right)^2} = \sqrt{\frac{{\sigma_M}^2}{N\langle M \rangle^2} + \left(\frac{1}{\sqrt{N}}\right)^2} = \frac{1}{\sqrt{C}}\sqrt{\frac{{\sigma_M}^2 + \langle M \rangle^2}{\langle M \rangle}} \quad (12).$$

Note that the relative uncertainty of the recorded counts is not just $1/\sqrt{C}$, which is simply expected from Poisson statistics, but should be multiplied with the factor shown in Eq. (12).

3.3 Validation

First, Figure 3 shows an example of the open beam TOF spectrum with the uncertainty determined by the procedures described above. From the enlarged plots Fig. 3 b), the expected uncertainty values are consistent with actual fluctuation. In order to quantitatively validate the procedures, we evaluated the fluctuation characteristics in several repeated measurements under the same condition. The uncertainty

discussed above can be expected from a single measurement based on counting statistics. This expected uncertainty should be consistent with the standard deviation obtained from repeated measurements under the same condition. Open beam images with the acquisition time of 1 min were repeatedly measured 10 times at the Larmor beamline, in which the flux was 5×10^6 n/cm^2/s. The same shutter periods were selected as for the spectra in Fig. 1. Figure 4 shows comparisons between the expected relative standard deviations from the above procedure and the deviations evaluated from the repeated measurements. These deviations were evaluated for the corrected neutron counts in a time bin at the almost beginning of the first shutter, at which TOF = 10.5 ms. In order to check the dependence of these deviation on counting statistics, these counts were integrated for various sizes of regions of interest. The expected deviations with no account of the multiple counting effect are also plotted. Although the standard deviation values from the repeated measurements are quite scattered due to its small number of trials, the expected values are consistent with the actual ones under various statistical conditions. Since the deviations with no account of the multiple counting effect are systematically underestimated, this effect should be considered to reasonably evaluate the uncertainty. Finally, we check the contribution of the overlap correction. In Fig. 3 a), we see no significant difference between the relative standard deviations with/without the correction. In this case, although the pixel occupation probability $P_{ocp}(t_i)$ was more than 60% at the end of the first shutter period (TOF=24.5 ms), the uncertainty can be expected from simple counting statistics. This is consistent with the prediction discussed above, because $N(t_i)/S$, which stands for the maximum correction contribution to the uncertainty, was less than 5×10^{-3} in this case. In addition, we confirmed that the counting statistics has stronger contribution to the uncertainty than the overlap correction. This also means that, if pixels are almost fully occupied and the recorded counts become close to zero, the uncertainty based on the counting statistics becomes quite large. From this point of view, the shutter periods should be carefully selected to avoid severe occupation of pixels and to keep the expected uncertainty to less than the required level.

4. Memory effects

4.1 Characteristics of memory effects

Since the detector stability is a very important characteristic for quantitative data analysis, we investigated the time trend of the detection efficiency of the MCP/Timepix detector. If the neutron beam intensity is constant, the open beam images should not be changing for a time-independent detection efficiency. Comparisons of open beam images is the simplest check of the detector stability. For this purpose, acquired images in tomography measurements could be a reasonable data set, because total measurement times are long and usually several open beam images are acquired for checking purposes. Figure 5 shows an experimental schedule of tomography measurements used in this comparison. In this experiment, 90 measurements with 40 min each, which means that the total measurement time was 60 hours, were conducted at the Larmor beam line with a flux of $5x10^6$ n/cm^2/s. The sample was a steel cylinder with 26 mm diameter and 20 mm height. For the tomography acquisition, the sample was rotated along the vertical cylinder axis, and 75 projection images were acquired for 50 hours in total. The projection images were very similar because the sample was axially symmetric. Before and after the sample projection measurements, several open beam images were acquired. At the end, additional cylinder sample projections were measured with two different views, which were side and cross sectional views. In the analysis discussed in this section, white beam images, which is integrated for the entire TOF range, are taken into account to evaluate the relative long-term stability.

Since the MCP/Timepix detector is expected to have a some fixed-pattern pixel-to-pixel distortions due to MCP structure and the neutron beam itself is not perfectly uniform, the images should be normalized with a given open beam image, especially if small differences are to be detected between different projections. Figure 6 a) shows an open beam image acquired after the tomography scan, and then normalized with another open beam image before the sample scan. The resulting, normalized image shows a relative change in the detection efficiency. We can recognize an obvious shadow or memory shape of the sample in this open beam or flat field image. This is a clear evidence of the memory effect in the MCP/Timepix detector. In order to discuss characteristics of the memory effect, temporal trends in the efficiency were investigated at various positions of the pixel matrix. Figure 7 shows temporal trends of the neutron counts at the center, top

right and bottom right positions, for which the regions of interest (ROIs) are also shown in Fig. 6. At the top right region, which was always outside the sample and fully irradiated over the entire period, the neutron counts first increased and then decreased gradually. At the center position, although the counts were quite low behind the sample, the counts started to increase again after the sample was removed. The bottom right position was first blocked with the sample during the tomography projections and then irradiated with the second open beam. This region was relatively freshly irradiated with the second open beam as well as the center position. After the second open beam, which was longer than the first one, this region was blocked with the sample once and then fully irradiated without the sample shielding again. At this region, the detection efficiency decreased while pixels were shielded by the sample, i.e. for reduced neutron irradiation. From these behaviors, the memory effect is considered to result from two different effects, related to an increase and a reduction of the detection efficiency.

The effect decreasing the efficiency in the MCP detector is well known as modification of inner surfaces of the MCP pores, which works as a secondary electron emitter in the electron multiplication process, due to intense electron impacts [16]. Since this effect deteriorates the MCP gain, the detection efficiency or the probability for signals exceeding the threshold level also decreases. This induces permanent damage in the MCP and is physically unrecoverable for the present generation of neutron sensitive MCP, although some promising new technology of MCP manufacturing substantially alleviates that problem. Since the electron impacts onto the inner surfaces of the MCP pores are proportional to the number of irradiated neutrons, the detection efficiency decreases with increasing neutron irradiation. For the current generation of MCPs the technical document from the manufacturer says that the MCP gain decreases by roughly 10% for the accumulated electron charge of 0.5 C/cm^2 [16]. Deterioration of the detection efficiency was experimentally evaluated to be roughly 5% for 70 hours neutron irradiation at the Larmor beamline with a flux of $5x10^6$ $n/cm^2/s$, for which the neutron fluence was 10^{12} n/cm^2. The accumulated electron charge for the irradiation was roughly 0.05 C/cm^2, assuming that a single neutron event generates $5x10^5$ electrons and the event generating probability is 50%. The expected gain deterioration is roughly 1%. However the relationship between the MCP gain and the detection efficiency may not be linear and is unknown.

Considering this ambiguity and individual characteristics of MCPs, this rough expectation is almost consistent with the experimental results shown in Fig. 7.

On the other hand, the effect increasing the efficiency is more complicated. The efficiency increases with the neutron irradiation and then saturates. However, if the irradiation is stopped or significantly reduced, the efficiency decreases again as shown at the bottom right region in Fig. 7. We have two possible models to explain this behavior. In the first possible model, "something" is charged up in the detector with neutron irradiation, causing an increase of the efficiency. Since this is simultaneously discharged with a certain time constant, the efficiency decreases once the irradiation is stopped . The second possibility is that "something" is deposited in the detector at first and this induces a decrease of the efficiency. One of the candidates of "something" is residual gas molecules. This can be scrubbed with neutron irradiation or multiplied electron impacts, causing an increase of the efficiency, and also re-deposit to the detector surface with a certain time constant. Given the small diameters of the MCP pores, the gas flow resistivity is also high. The scrubbed gas molecules, therefore, cannot easily move to the outside of the pores. Under this situation, this model has position dependency. In the both models, the efficiency increases with the neutron irradiation and decreases when the irradiation stops. We note that the charge-up model is more difficult to explain the efficiency rise. For example, electrons can be accumulated on the inner surfaces of MCP pores, preferentially near the bottom side of the MCP. As a consequence, the electric field inside the MCP pores is decreased and the MCP gain is lowered. In addition, since the resistivity on inner surfaces of the MCP pores is moderate, it is difficult to explain the long time constant observed in the experiments. On the other hand, we can more easily imagine that "something" disturbs the neutron detection and decreases the efficiency. In this paper, we attempted to explain the efficiency increase by using the second possibility.

4.2 Correction procedures

We propose the correction procedures for the memory effect assuming the model described above. Since various processes should be considered simultaneously, the following rate equations are applied:

$$C_i = \int_{t_{s,i}}^{t_{e,i}} A\, f(t)\varepsilon(t)dt \quad (13),$$

$$\varepsilon(t) = \varepsilon_0\, \varepsilon_D(t)\varepsilon_{SC}(t) \quad (14),$$

$$-\frac{d\varepsilon_D(t)}{\varepsilon_D(t)} = \tau_D dF = \tau_D\, f(t)dt \quad (15),$$

$$\varepsilon_{SC}(t) = 1-\alpha N(t) \quad (16),$$

$$\frac{dN(t)}{dt} = -\gamma\, f(t)N(t) + \tau_{RB}(1-N(t)) \quad (17),$$

where C_i; the recorded counts of i th measurement, $t_{s,i}$, $t_{e,i}$; start and end time of i th measurement, A; the pixel area, f(t); the neutron flux on the detector surface, ε(t); the detection efficiency, ε_0; the initial detection efficiency, ε_D(t), ε_{SC}(t); contribution factors of the permanent damage and the scrubbing effect in the detection efficiency, τ_D; the decay constant of the permanent damage, F; the irradiated neutron fluence, α; the efficiency reduction coefficient with the deposited molecules, N(t); the fraction of deposition, γ; the scrubbing coefficient, τ_{RB}; the re-deposition time constant. Eq. (15) stands for the permanent damage depending on the irradiated neutrons. Eq. (17) includes the scrubbing effect and "re-deposition effect" of the "something". Since the N(t) stands for the fraction of deposited surface, N(t)=1 means that the surface is fully deposited. Since the neutron flux f(t) on the detector surface depends on the sample transmittance T_i in i th measurement, this parameter can be written as:

$$f(t) = T_i\, f_0(t) = T_i\, B i_p(t) \quad (18),$$

where f_0(t); the flux without the sample, i_p(t); the proton current at the neutron source, B; the conversion constant from the proton current to the neutron flux. In our case, the proton current was used as relative neutron intensity instead of the absolute open beam neutron flux f_0(t).

By modifying Eq. (13), the modified transmittance T_i' in the i th measurement can be derived as follows:

$$T_i' = \varepsilon_0 T_i = \frac{C_i}{A\int_{t_i}^{t_{i+1}} f_0(t)\varepsilon_D(t)\varepsilon_{SC}(t)dt} \quad (13').$$

Eqs. (15) and (17) can also be rewritten as the following equations:

$$-\frac{d\varepsilon_D(t)}{\varepsilon_D(t)} = \frac{\tau_D}{\varepsilon_0}\varepsilon_0 T_i \; f_0(t)dt = \tau_D' \, T_i' \, f_0(t)dt \qquad (15'),$$

$$\frac{dN(t)}{dt} = -\frac{\gamma}{\varepsilon_0}\varepsilon_0 T_i \; f_0(t)N(t) + \tau_{RB}(1-N(t)) = -\gamma' T_i' \, f_0(t)N(t) + \tau_{RB}(1-N(t)) \qquad (17'),$$

where $\gamma'=\gamma/\varepsilon_0$ and $\tau_D'=\tau_D/\varepsilon_0$. We know the recorded counts C_i and the open beam flux $f_0(t)$, which is obtained from time trend of the proton beam current. The parameters τ_D', α, γ' and τ_{RB} should be constant and are tuning parameters in the correction procedure. The initial values $\varepsilon_D(0)$ and $\varepsilon_{SC}(0)$ can be unity at the beginning of the measurement. The transmittance T_i or T_i' in i th measurement is usually an unknown factor and $\varepsilon_D(t)$ and $\varepsilon_{SC}(t)$ also depend on T_i'. However, once T_i' is fixed, $\varepsilon_D(t)$ and $\varepsilon_{SC}(t)$ can be calculated numerically by using (15'), (16) and (17'). The dominator of Eq. (13') can also be integrated numerically. By repeating these procedures in the i th measurement, we can iteratively determine the modified transmittance T_i'. The transmittance T_i should be unity for all open beam measurements. This means that the modified transmittance T_i' should be constant even if ε_0 is unknown. The parameters τ_D', α, γ' and τ_{RB} must be tuned to realize this limitation. Note that if ε_0 is unknown, these parameters can be tuned. Following this parameter tuning procedure, one can obtain the initial detection efficiency ε_0 as the constant value of T_i' in the open beam measurements. This tuning procedure might be automatically performed but we have applied a manual tuning process based on a trial and error approach in this paper. As a future work, we aim to develop an automated parameter tuning algorithm. In principle, the initial deposition fraction $N(0)$ should be unity. However, this value might be reduced by unknown neutron irradiation before starting a measurement. For example, we usually irradiated the detector without data recording for detector position alignment purposes before a measurement. The parameter $N(0)$ can also be determined iteratively in the processes described above. The purpose of measurements is usually to obtain the transmittance of samples. The final outcome in the above procedures is the modified transmittance T_i', which is the product of the transmittance T_i and the initial detection efficiency ε_0. Since the initial efficiency ε_0 might depend on the position in the detector, we can obtain the corrected transmittance images by normalizing with an image of

the open beam measurement.

In principle, the consideration based on the rate equations should be taken into account for intervals between each measurement, in which no neutron count is recorded usually. This means that we have no information for determination of the sample transmittance in the intervals between the measurements. In order to specify the situation, ideally, the detector entrance window should be fully shielded as soon as possible after the measurement is finished, because we used the accelerator proton current instead of the real open beam neutron flux $f_0(t)$. For the measurements presented in this paper, the detector was irradiated for some intervals but shielded at other times. Therefore, we used zero transmittance for the shielded intervals and the transmittance used in the previous measurement for the irradiated ones. Since the irradiated intervals were relatively short compared with the characteristic time constants in the memory effect, no significant error is introduced from this process.

4.3 Corrected results

After the manual parameter tuning procedures, we determined the parameters listed in Table 1. Figure 8 shows temporal trends of the calculated variables in the rate equations at the end of each measurement run. The amount of the deposited molecules decreases during the neutron irradiation and reaches the equilibrium condition depending on the irradiated flux. The detection efficiency was determined based on this deposited molecule amount and the permanent damage behavior. The temporal trends of the efficiency are consistent with the recorded neutron counts shown in Fig. 7. Consequently, we obtained almost constant values of the modified transmittance T_i' for the open beam measurements. The initial detection efficiency ε_0, additionally, can be estimated to be 0.075 from the modified transmittance for the open beam measurements, because T_i' is defined as $\varepsilon_0 T_i$. This value is roughly consistent with the efficiency determined in the other measurement. Note that this efficiency is not for neutrons in the entire spectrum but only for neutrons used in these measurements, which were with the wavelength from 1.5 to 5 angstrom. Since the initial detection efficiency shows also a position-dependent variation, the corrected

transmittance images can be obtained by normalizing with the modified transmittance image in a certain open beam measurement. Figure 6 b) shows the corrected transmittance image. The memory effect can significantly be reduced by the proposed correction procedures. In this case, the standard deviation of the transmittance for all open beam measurements was improved from 2% to 0.3% with the correction. We note that the scrubbing model is one of the candidates to explain the efficiency increase. However, the typical behavior of the memory effect have been well characterized through this kind of analysis.

5. Conclusions

We discussed the uncertainty and the stability of the neutron sensitive MCP/Timepix detector when operated in the event timing mode for energy-resolved quantitative analysis at the ISIS pulsed neutron source. Under relatively high neutron flux of more than 10^6 n/cm^2/s, the counting loss or the overlap effect becomes significant and should be corrected. The contribution of this correction procedure to the uncertainty was concluded to be negligible from considerations based on the error propagation even if the pixel occupation probability is more than 50%. This means that the dominant component to the uncertainty arises from the counting statistics. However, for experiments where shutter lengths are too long and the pixel occupation probability reaches nearly 100%, the number of recorded counts becomes small resulting in poor counting statistics which would be a significant problem. Therefore shutter lengths should be carefully chosen, i.e. shorter ones for high-flux time-of-flight regions. This limitation will not be present in the next generation of Timepix readout, which has a sparsified event output and no readout gaps. In the event timing mode, we, additionally, have to take into account the multiple counting effect, in which a single neutron event might induce multiple counts over neighboring pixels, in consideration of the counting statistics.

The detection efficiency of this detector changes gradually under relatively high neutron flux due to the ageing effects of Microchannel Plates. Since this change is position-dependent, this effect induces the memory image. This efficiency change comes from two reasons: the permanent damage and the scrubbing effect, in which “something” disturbing the neutron detection is deposited in the detector and scrubbed with

the neutron irradiation or the multiplied electron impacts. At a moment, the origin of the scrubbing effect is unknown but identification of its origin would be a future work. However, the memory effect can be significantly reduced with the correction procedures using the rate equations taking accounts of the damage and the scrubbing effect. The typical behavior of the memory effect has been well characterized through the analysis. The parameters used in the correction procedures were manually tuned through a large number of trail-and-error attempts. Future work will focus on developing automated parameter tuning algorithm as part of the standard image analysis.

Acknowledgements

This work is partially supported by JSPS Program for Advancing Strategic International Networks to Accelerate the Circulation of Talented Researchers.

References

[1] T. Shinohara, T. Kai, "Commissioning start of Energy-Resolved Neutron Imaging System, RADEN in J-PARC", Neutron News, **26**, 11-14 (2015).

[2] T. Minniti, W. Kockelmann, G. Burca, J.F. Kelleher, S. Kabra, S.Y. Zhang, D.E. Pooley, E.M. Schooneveld, Q. Mutamba, J. Sykora, N.J. Rhodes, F.M. Pouzols, J.B. Nightingale, F. Aliotta, L.M. Bonaccorsi, R. Ponterio, G. Salvato, S. Trusso, C. Vasi, A.S. Tremsin, G. Gorini, "Materials analysis opportunities on the new neutron imaging facility IMAT@ISIS ",Journal of Instrumentation, **11**, C03014 (2016).

[3] W. Kockelmann, G. Frei, E.H. Lehmann, P. Vontobel, J.R. Santisteban, "Energy-selective neutron transmission imaging at a pulsed source" Nuclear Instruments and Methods, **A578**, 421-434 (2007).

[4] M. Strobl, "Future prospects of imaging at spallation neutron sources", Nuclear Instruments and

Methods, A604, 646-652 (2009).

[5] A.S. Tremsin, V. Dangendorf, K. Tittelmeier, B. Schillinger, M. Schulz, M. Lerche, W.B. Feller, ”Time-resolved neutron imaging at ANTARES cold neutron beamline”, Journal of Instrumentation, **10**, P07008 (2015).

[6] A.S. Tremsin, J.V. Vallerga, J.B. McPhate, O.H.W. Siegmund, ”Optimization of high count rate event counting detector with Microchannel Plates and quad Timepix readout”, Nuclear Instruments and Methods, **A787**, 20-25 (2015).

[7] A.S. Tremsin, M. Morgano, T. Panzner, E. Lehmann, U. Filgers, J.V. Vallerga, J.B. McPhate, O.H.W. Siegmund, W.B. Feller, ”High resolution neutron imaging capabilities at BOA beamline at Paul Scherrer Institut”, Nuclear Instruments and Methods, **A784**, 486-493 (2015).

[8] A.S. Tremsin, J.B. McPhate, J.V. Vallerga, O.H.W. Siegmund, J.S. Hull, W.B. Feller, E. Lehmann, ” High-resolution neutron radiography with microchannel plates: Proof-of-principle experiments at PSI”, Nuclear Instruments and Methods, **A605**, 103-106 (2009)

[9] A.S. Tremsin, J.B. McPhate, J.V. Vallerga, O.H.W. Siegmund, W. Kockelmann, E.M. Schooneveld, N.J. Rhodes, W.B. Feller, ” High Resolution Neutron Resonance Absorption Imaging at a Pulsed Neutron Beamline”, IEEE Transaction on Nuclear Science, **59**, 3272-3277 (2012)

[10] A.S. Tremsin, J.B. McPhate, J.V. Vallerga, O.H.W. Siegmund, W. Kockelmann, A. Steuwer, W.B. Feller, ” High-Resolution Neutron Counting Sensor in Strain Mapping Through Transmission Bragg Edge Diffraction”, IEEE Sensors Journal, **11,** 3433-3436 (2011).

[11] A.S. Tremsin, J.V. Vallerga, J.B. McPhate, O.H.W. Siegmund, “Optimization of Timepix count rate capabilities for the applications with a periodic input signal”, Journal of Instrumentation, **9**, C05026 (2014).

[12] S.E. Sobottka, M.B. Williams, “Delay line readout of microchannel plates”, IEEE Transactions on Nuclear Science, **35**, 348-351 (1988).

[13] O. Jagutzki, V. Mergel, K. Ullmann-Pfleger, L. Spielberger, U. Spillmann, R. Dorner, H.

Schmidt-Bocking, " A broad-application microchannel-plate detector system for advanced particle or photon detection tasks: large area imaging, precise multi-hit timing information and high detection rate" Nuclear Instruments and Methods, A**477**, 244-249 (2002).

[14] A.S. Tremsin, J.V. Vallerga, J.B. McPhate, O.H.W. Siegmund, R. Raffanti, "High Resolution Photon Counting With MCP-Timepix Quad Parallel Readout Operating at >1KHz Frame Rates", IEEE Transactions on Nuclear Science, **60**, 578-585 (2013)

[15] X. Llopart, R. Ballabriga, M. Campbell, L. Tlustos, W. Wong, "Timepix, a 65k programmable pixel readout chip for arrival time, energy and/or photon counting measurements", Nuclear Instruments and Methods, **A581**, 485-494 (2007)

[16] Hamamatsu Photonics K.K., "Technical information - MCP Assembly", TMCP9002E01

Table Captions

Table 1 The parameters used in the correction procedures.

Table 1 The parameters used in the correction procedures.

A	0.0055 cm x 0.0055 cm = 3.025×10^{-5} cm^2
B	5×10^6 $(n/cm^2/s)/40$ μA = 1.25×10^5 $(n/cm^2/s)/\mu A$
$\tau_D' = \tau_D/\varepsilon_0$	1.2×10^{-12} $(n/cm^2)^{-1}$ = 9.0×10^{-14} $(n/cm^2)^{-1}/0.075$
$\gamma' = \gamma/\varepsilon_0$	1.0×10^{-10} $(n/cm^2)^{-1}$ = 7.5×10^{-12} $(n/cm^2)^{-1}/0.075$
τ_{RC}	1.0×10^{-5} s^{-1}
α	0.17

Figure Captions

Figure 1 a) Open beam TOF spectra obtained at Larmor with the neutron sensitive MCP/Timepix detector and b) its enlarged plot near a readout gap. Three shutter periods (10 to 24.7, 25 to 39.7, 40 to 50.7 ms) were selected. The estimated integrated neutron flux was $5x10^6$ $n/cm^2/s$.

Figure 2 An example image of the multiple counting effect. In this image, separately distributed neutron events are obtained due to a very short acquisition time of 1 seconds. a) Entire field of view. b) Enlarged image for the small square in Fig. 2 a).

Figure 3 a) Open beam TOF spectrum with the uncertainty determined by the proposed procedures and b) its enlarged plot for the corrected spectrum.

Figure 4 Comparisons between the expected relative standard deviations and the deviations evaluated from repeated measurements. In order to check the dependence on counting statistics, relative uncertainties were extracted by summation over increasing region of interest (ROI), i.e. pixel numbers.

Figure 5 An experimental schedule of tomography measurements and the sample photograph. The sample was a steel cylinder with 26 mm diameter and 20 mm long. The collection time was 40 min for each measurement.

Figure 6 a) An open beam image acquired after the tomography scan and normalized with a different open beam image collected before the tomography scan. b) The corrected transmittance image obtained from the same measurements. The squares at the center, top right and bottom right show the regions of interest (ROIs) for temporal trends of the neutron counts shown in Fig. 7.

Figure 7 Temporal trends of the neutron counts at the center, top right and bottom right squares shown

in Fig. 6. a) Overall plots, b) Enlarged plots. Open dots; Open beam. Closed dots; Shielded with the sample.

Figure 8 Temporal trends of the calculated variables in the rate equations at the end of each measurement run. a) The deposition fraction $N(t_{e,i})$, b) The normalized detection efficiency $\varepsilon(t_{e,i})/\varepsilon_0$, c) The modified transmittance T_i'.

a)

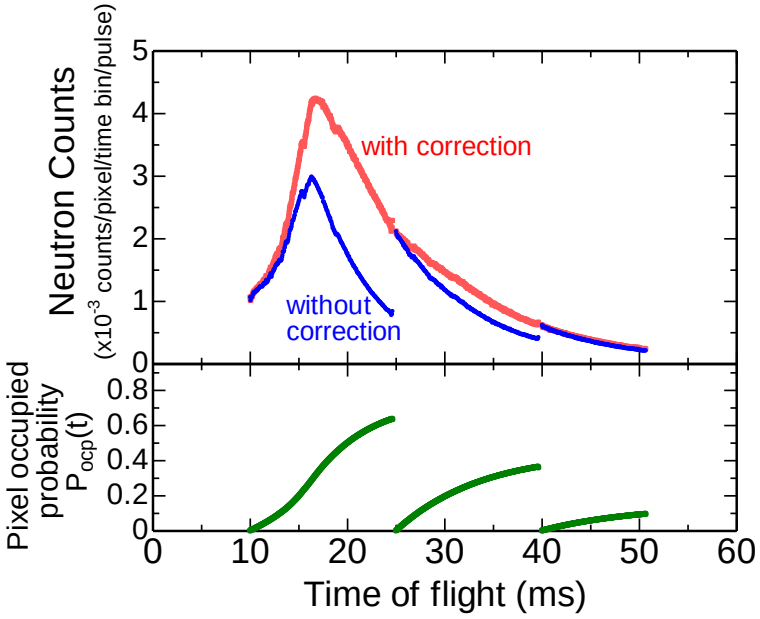

b)

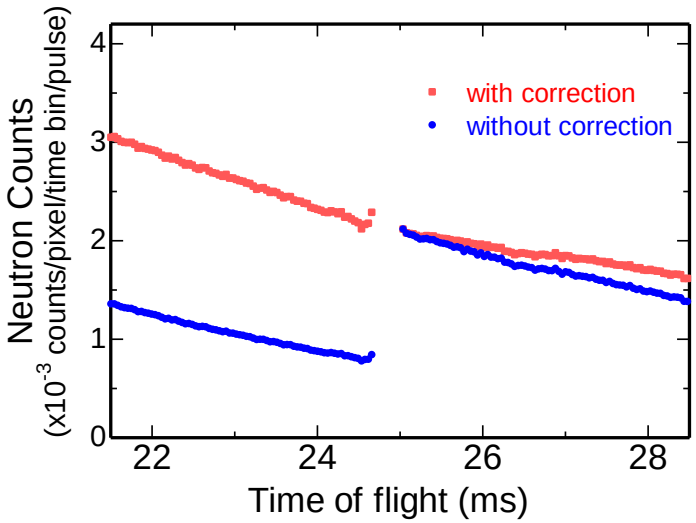

Figure 1 a) Open beam TOF spectra obtained at Larmor with the neutron sensitive MCP/Timepix detector and b) its enlarged plot near a readout gap. Three shutter periods (10 to 24.7, 25 to 39.7, 40 to 50.7 ms) were selected. The estimated integrated neutron flux was 5×10^6 n/cm^2/s.

a) b)

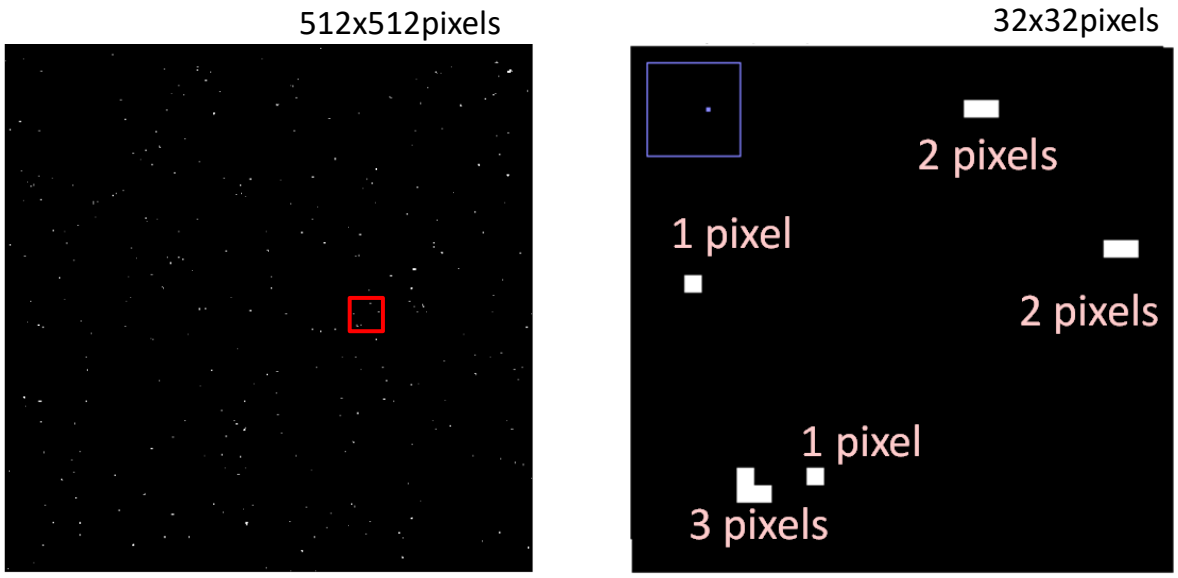

Figure 2 An example image of the multiple counting effect. In this image, separately distributed neutron events are obtained due to a very short acquisition time of 1 second. a) Entire field of view. b) Enlarged image for the small square in Fig. 2 a).

a)

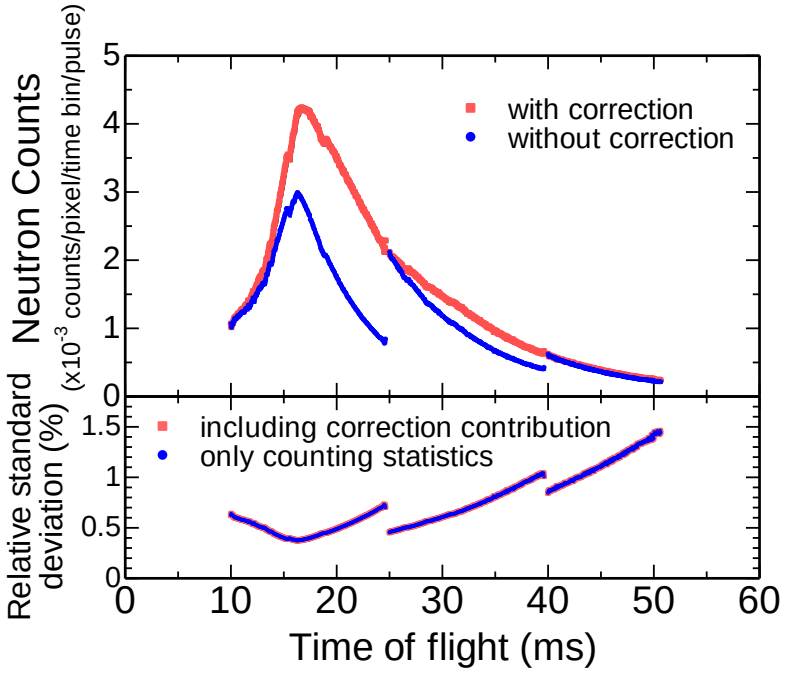

b)

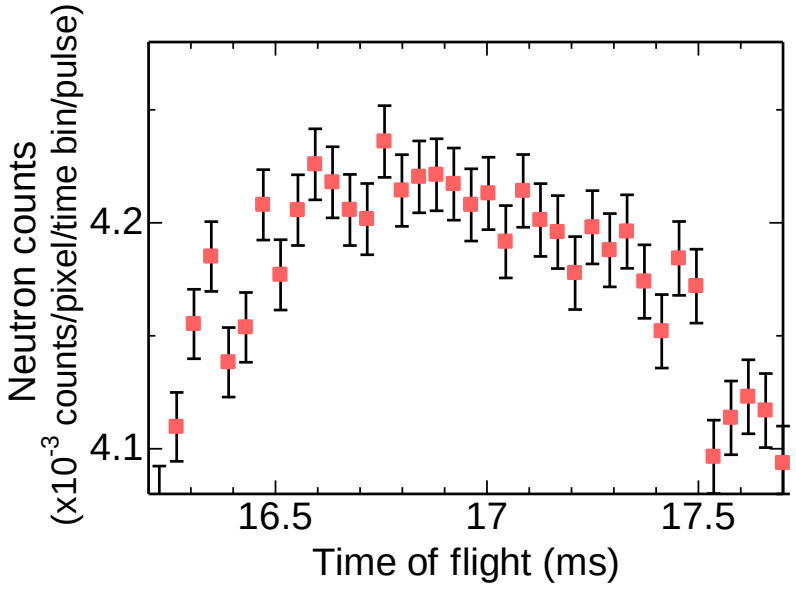

Figure 3 a) Open beam TOF spectrum with the uncertainty determined by the proposed procedures and b) its enlarged plot for the corrected spectrum.

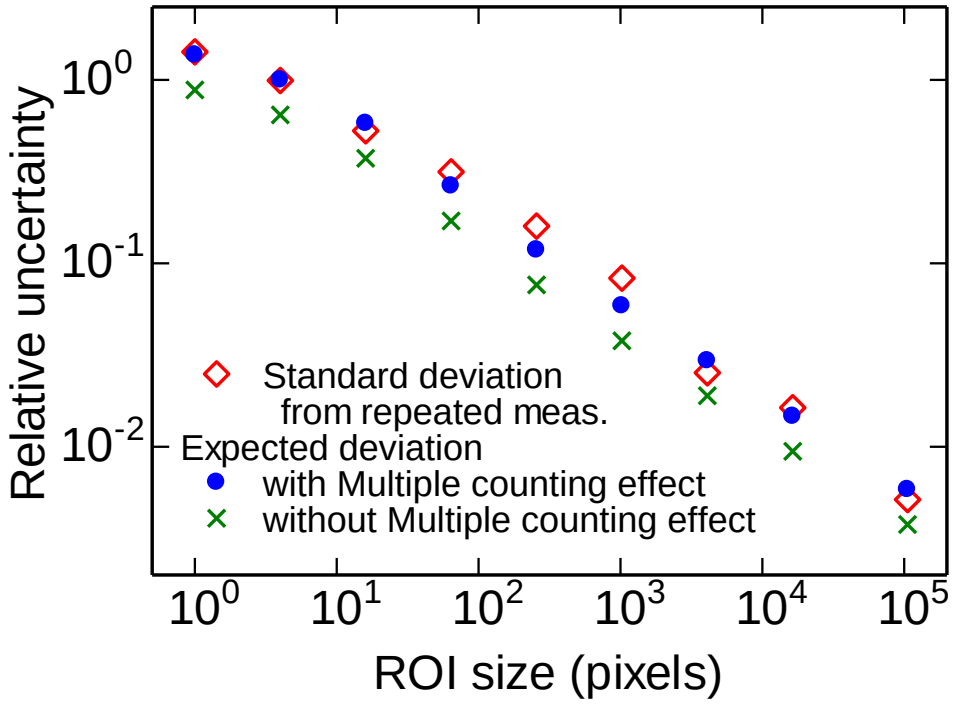

Figure 4 Comparisons between the expected relative standard deviations and the deviations evaluated from repeated measurements. In order to check the dependence on counting statistics, relative uncertainties were extracted by summation over increasing region of interest (ROI), i.e. pixel numbers.

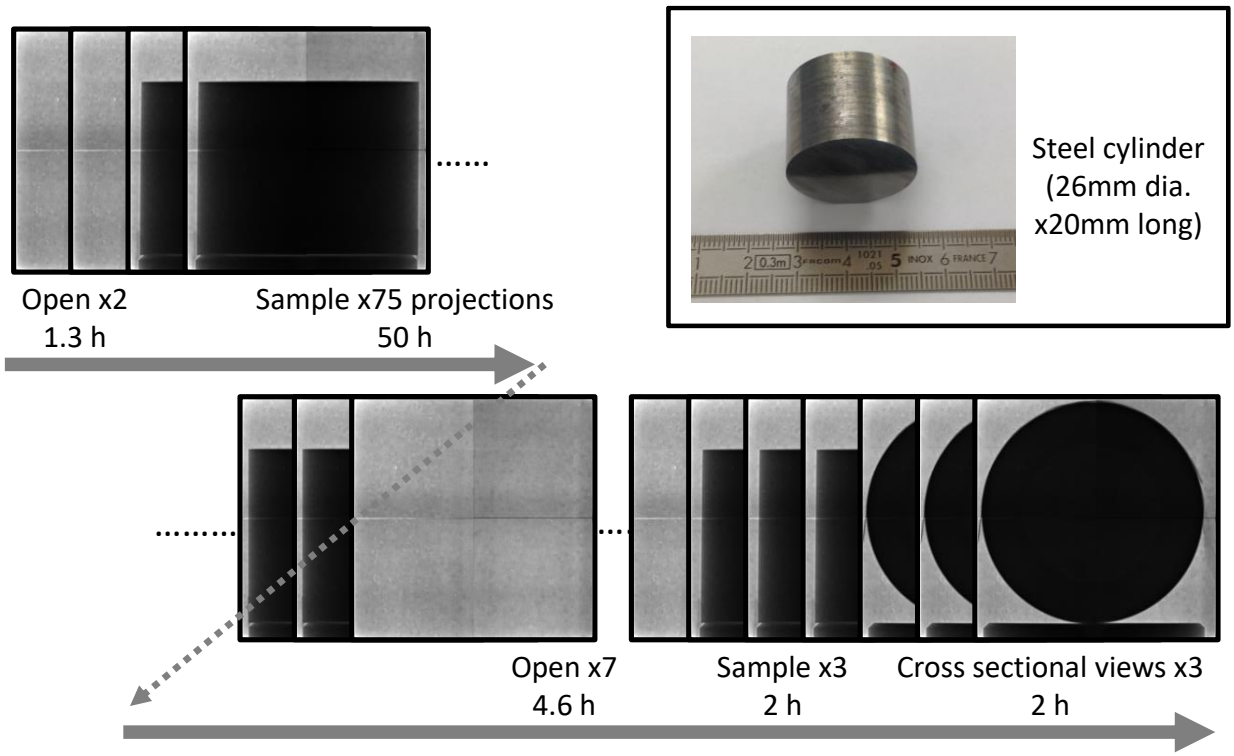

Figure 5 An experimental schedule of tomography measurements and the sample photograph. The sample was a steel cylinder with 26 mm diameter and 20 mm long. The collection time was 40 min for each measurement.

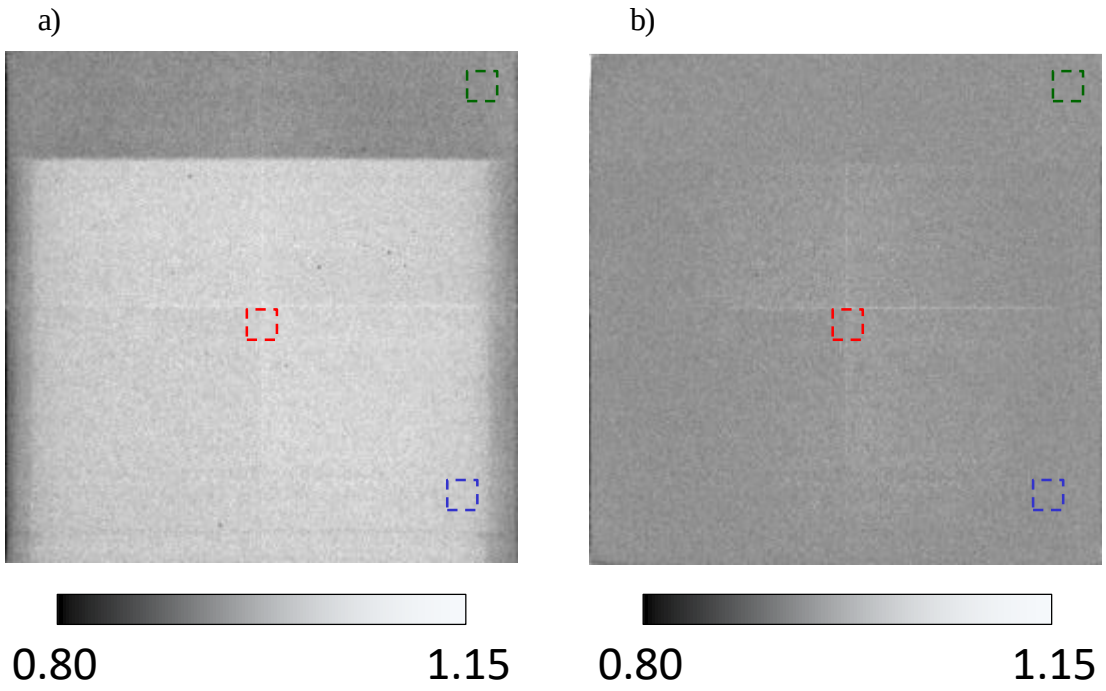

Figure 6 a) An open beam image acquired after the tomography scan and normalized with a different open beam image collected before the tomography scan. b) The corrected transmittance image obtained from the same measurements. The squares at the center, top right and bottom right show the regions of interest (ROIs) for temporal trends of the neutron counts shown in Fig. 7.

a)

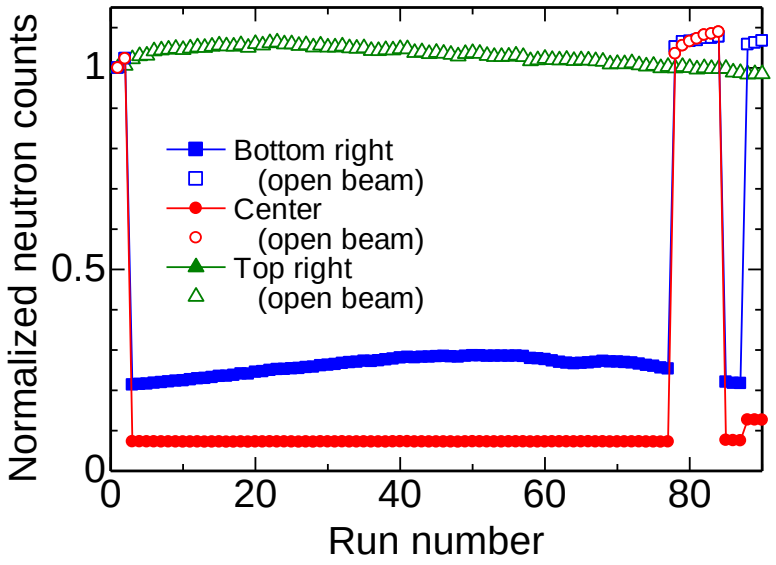

b)

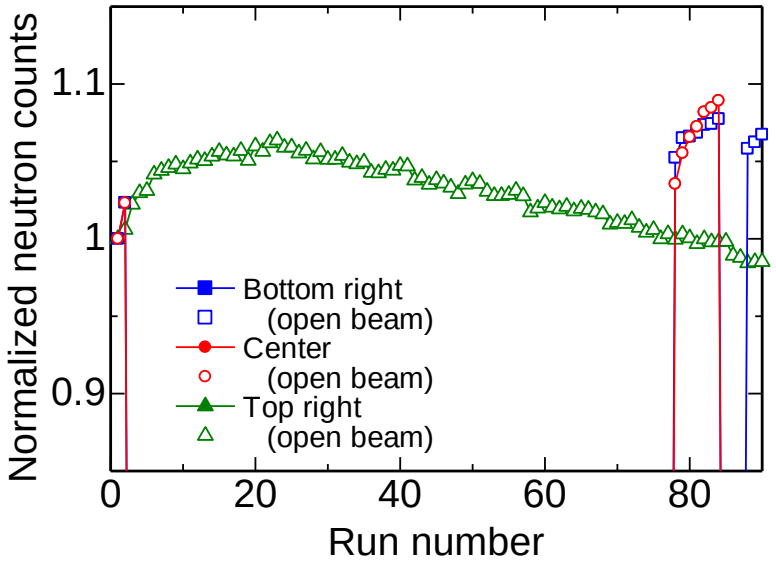

Figure 7 Temporal trends of the neutron counts at the center, top right and bottom right squares shown in Fig. 6. a) Overall plots, b) Enlarged plots. Open dots; Open beam. Closed dots; Shielded with the sample.

a)

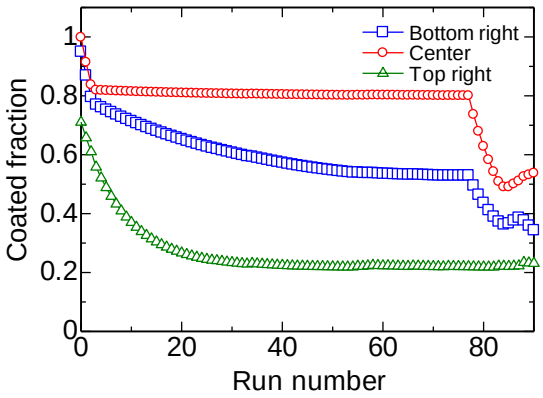

b)

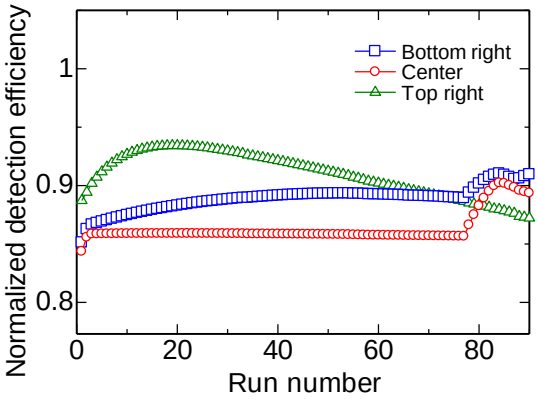

c)

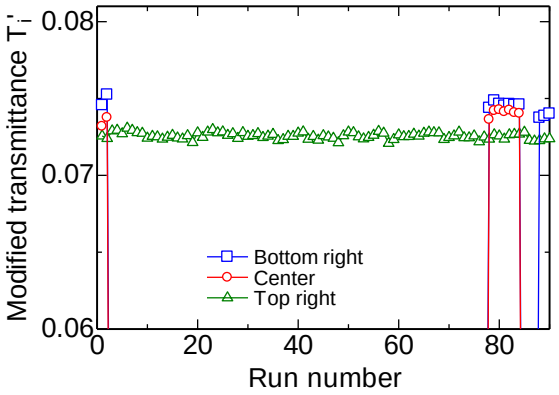

Figure 8 Temporal trends of the calculated variables in the rate equations at the end of each measurement run. a) The deposition fraction $N(t_{e,i})$, b) The normalized detection efficiency $\varepsilon(t_{e,i})/\varepsilon_0$, c) The modified transmittance T_i'.